

MinD the gap: Membrane proteins form 3D patterns in a suspension of liposomes

Amelie Chardac,¹ Michael M. Norton,¹ Jonathan Touboul,² and Guillaume Duclos^{1,*}

¹*Department of Physics, Brandeis University, 415 South street, Waltham, MA 02453*

²*Department of Mathematics and Volen National Center for Complex Systems, Brandeis University, 415 South street, Waltham, MA 02453*

The self-organization of pattern-forming systems depends not only on the chemical but also physical properties of their components. In this work, we fragmented and dispersed the MinDE protein system's lipid substrate into diffusive sub-micrometer-sized liposomes, and report that the ATP-fueled protein-protein interactions continue to drive spatially extended patterns at scales well separated from those of the requisite liposomes, despite the complete loss of membrane continuity. The patterns form in three-dimensions because the membrane is dispersed in a volume. By varying protein concentration, liposome size distribution, and density, we observed and characterized rich 3D dynamical patterns at steady state, including traveling waves, dynamical spirals and a mixed phase where both patterns coexist. Simulations and linear stability analysis of a coarse-grained model reveal that the dispersed membranes's physical properties effectively rescale two key factors that govern pattern formation and wavelength selection: protein-membrane binding rates and diffusion. This work highlights the robustness of pattern formation in membrane-bulk systems despite membrane fragmentation. It suggests that biological protein systems have the potential to serve as adaptable templates for out-of-equilibrium self-organization in 3D, beyond *in vivo* biological contexts.

I. INTRODUCTION

Pattern formation via reaction-diffusion is a fundamental self-organizing principle that regulates a variety of biological processes across scales [1–3]. In cells, pattern-forming protein-protein interactions are often hosted by structurally complex environments. Pattern-forming proteins often interact with a substrate, which can either be two-dimensional and continuous, like the plasma membrane [4–9], or discontinuous and dispersed in three-dimension, like the coiled nucleosome [10–13] or the actin cortex [14–16]. Furthermore, while membrane proteins can form patterns on continuous substrates that extend further than one pattern's wavelength, the presence of a myriad of small diffusive vesicles dispersed within the cell cytoplasm begs the question: Would patterns still form if the membrane was discontinuous, scattered into highly diffusive liposomes with a characteristic size multiple orders of magnitude smaller than a wavelength? We propose to address this puzzle using the MinDE system.

The spatiotemporal oscillations of the MinDE proteins on the membrane of *E. Coli* has served as a paradigmatic model system to study pattern formation *in vivo* [4–7] and *in vitro* [9, 17]. *In vivo*, the pole-to-pole oscillations of MinD lead to the robust assembly of a cytokinetic ring of FtsZ polymers in the middle of the bacterium, ensuring the formation of two daughter cells of the same size [7]. *In vitro*, MinDE complexes form a variety of dynamic and static patterns on continuous lipid membranes [18], which can template the self-organization of other membrane-bound proteins [19], cargos [20, 21], or drive the transport of cell-sized liposomes [22].

The MinDE system is peculiar among well-studied synthetic reaction-diffusion systems, such as the Belousov-Zhabotinsky [23, 24] or Iodine clock reactions [25, 26], because of the mixed 2D-3D nature of its dynamics. While protein patterns form on a 2D membrane, the dynamics taking place in the adjoining 3D bulk fluid critically shape their spatiotemporal properties. Recent experimental and theoretical work has shown that geometry, membrane curvature, and the local cytosol-to-membrane ratio modulate pattern formation [3, 27–31]. The impact of transport in the cytosol on membrane pattern formation was further established in experiments and simulations on discontinuous membranes - either two opposing lipid membranes separated by a thin gap or arrays of coplanar islands - demonstrating that cytosol-mediated coupling can lead to pattern synchronization on 2D membranes [32, 33]. Thus, while the apparent patterns are localized to the 2D membrane, understanding the spatiotemporal dynamics in the 3D bulk is essential for explaining why and what types of patterns form.

In this paper, we leverage the cytosolic coupling to extend the Min system beyond its native configuration, examining its ability to form patterns in a 3D reactive fluid, where the membrane is not only discontinuous but dispersed and freely diffusing within a 3D fluid. Combining experiments, simulations, and linear stability analysis of a coarse-grained model we reveal that the MinDE proteins can form 3D dynamical patterns when they interact in a suspension of dispersed, freely diffusing, submicrometer-spaced liposomes. We find that the fragmented lipid membrane can be recast as another reactive species in the Min reaction system. While sufficient lipids are needed to facilitate the protein-protein interaction, membrane continuity is not necessary for Min protein patterns to form. The discontinuous membrane enables the study of MinDE pattern formation in 3D,

* gduclos@brandeis.edu

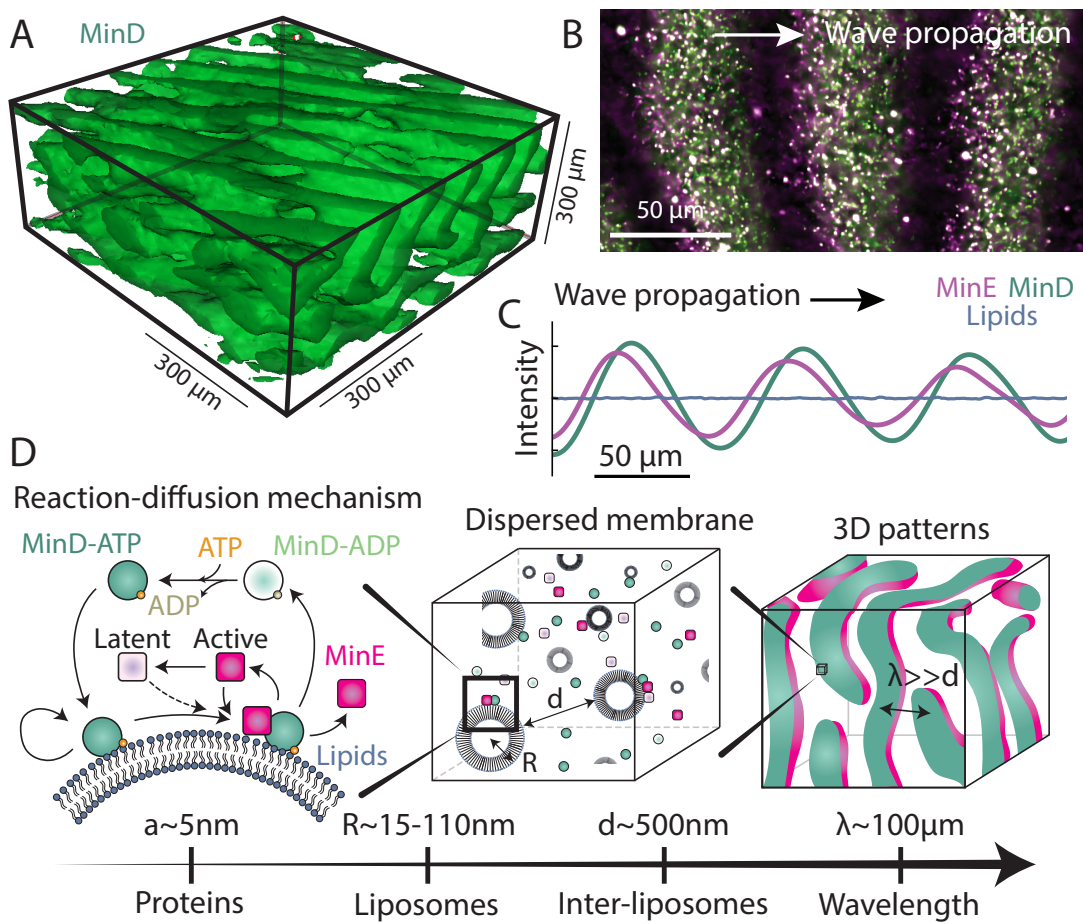


FIG. 1. **The formation of 3D patterns on a dispersed membrane is a multiscale phenomena.** (A) 3D reconstruction of dynamical patterns of MinD proteins from confocal microscopy. (B) Confocal slice of MinD (green) and MinE (magenta) forming traveling waves on the dispersed membrane. The largest lipid vesicles onto which proteins are bound are visible using fluorescence microscopy. The mean liposomes' radius is 15 nm. (C) Intensity profile of MinD (green), MinE (magenta), and the lipids (blue) along the direction of propagation of the wave (black arrow). MinE is located at the rear of the waves, following MinD. The lipids are spatially homogeneous. (D) Schematic of the chemical reaction network between MinD, MinE, ATP, and the dispersed membrane. The typical wavelength λ of the traveling waves is significantly larger than the size R of individual liposomes and the inter-liposome distance d .

revealing novel dynamical phases that are qualitatively distinct from the patterns observed on a 2D membrane.

II. 3D LARGE-SCALE PATTERNS FORM ON A SUSPENSION OF SUBMICROMETER-SIZED LIPOSOMES.

In this article, we investigate the mechanisms that control the formation of 3D patterns on a dispersed substrate using the Min system from *E. Coli* [4, 34, 35]. Our *in vitro* model system consists of two proteins, MinD and MinE, a source of chemical energy, Adenosine Triphosphate (ATP), that drives the oscillatory chemical reaction, and a spatially homogeneous suspension of liposomes with a mean radius ranging from 15 to 110 nm (see Methods B). Consequently, the substrate on which the protein-protein interaction occurs is discontinuous,

curved, three-dimensional, and can diffuse isotropically. The biochemical mechanisms that lead to the formation of patterns on a flat 2D lipid bilayer are well established [3, 9, 36]. Upon binding to ATP, MinD spontaneously dimerizes, which enhances its ability to insert itself within a lipid membrane. MinE binds to membrane-bound MinD, triggering ATP's hydrolysis by MinD and the subsequent detachment of MinD from the membrane. In turn, MinE can then detach from the membrane and enters the solution, where it will rapidly transition from an active configuration in which it can rapidly bind to another MinD, to a latent conformation with a lower MinD affinity [36]. The cycle is complete when MinD exchanges its bound ADP for another ATP molecule (Fig. 1D).

Here, we report that MinE and MinD form dynamical patterns in 3D in the liposomes suspension. Confocal microscopy revealed that MinD protein patterns form and move in all directions, spanning the system size (Fig. 1A,

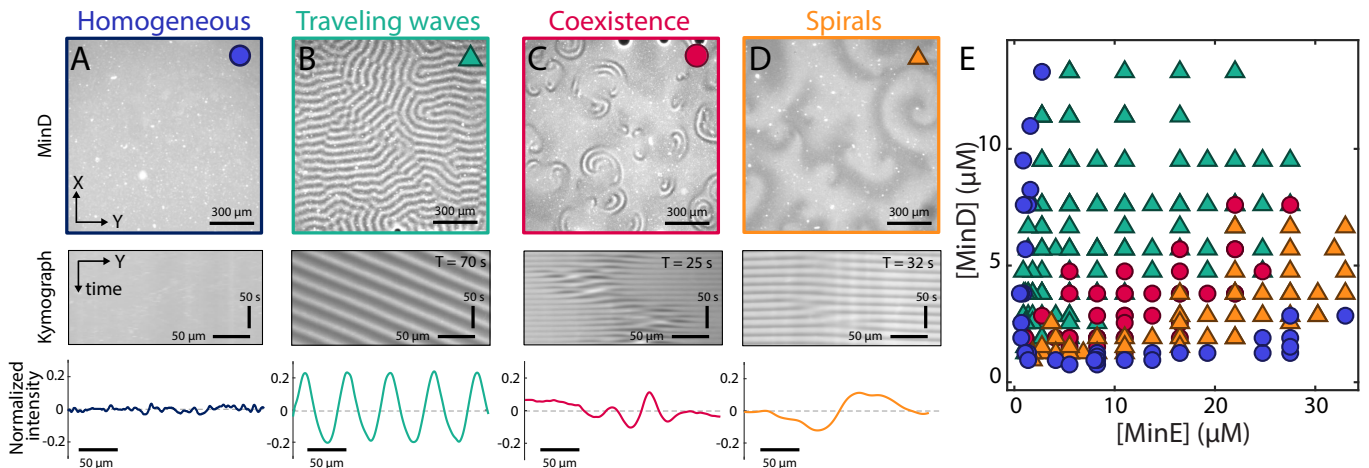


FIG. 2. **Proteins concentrations regulate pattern selection.** (A) Homogeneous steady-state, (B) Traveling waves, (C) Coexistence phase, (D) Spiral phase. The top row shows the fluorescence images of MinD (Widefield microscopy), the middle row shows kymographs (space-time plots) of the pattern, and the bottom row shows the normalized MinD fluorescence intensity along a line. (E) Experimental phase diagram where the concentrations of MinD and MinE are changed. Each data point represents two to five replicates. For all those experiments, the liposomes suspension properties are kept constant: $R = 15$ nm and $c_o = 0.4$ mM.

Fig. S2 and Movie 1). Fluorescent labeling of the proteins and lipids revealed that i) MinE trails behind MinD (Fig. 1B-C), consistent with MinDE patterns on continuous membranes [37] and ii) the lipids are homogeneously distributed in 3D (Fig. 1C, Fig. S3).

Importantly, the length scales at play in this oscillatory reaction span over multiple orders of magnitude (Fig. 1D): the liposome mean radius range from 15 nm to 110 nm depending on the preparation protocol (Fig. S1); the spacing between liposomes ranges from 50 nm to around 2 μ m; finally, the wavelength of the patterns varies between 50 and 100 μ m, spanning, typically, hundreds to a thousand vesicles. These observations prompted us to further identify the physical mechanisms and relevant lengthscales that contribute to the formation of dynamical patterns in 3D.

III. PROTEINS CONCENTRATIONS REGULATE PATTERN SELECTION

We first investigated the impact of protein concentrations on pattern formation. We identified a variety of distinct dynamical phases whose structure and dynamics were characterized through their kymographs and intensity profiles Fig. 2: traveling waves, spirals, and a coexistence phase. Titrating the concentrations of MinD and MinE revealed that the patterns are controlled by the proteins concentrations (Fig. 2E). A critical concentration of both proteins is necessary to destabilize the homogeneous steady state (Fig. 2A). Patterns form for a range of protein concentrations spanning over a decade, revealing the robustness of pattern formation in this system. Traveling waves dominate when MinD is in excess

compared to MinE. In that phase, multiple domains in which planar waves propagate in different directions coexist (Fig. 2B, Movie S1). The characteristic size of each domain is around a few wavelength in length. The direction of propagation is discontinuous at the boundary between two domains (Fig. S4). The domains reorganize over timescales much longer than the typical oscillation period. Spirals patterns dominate when MinE is in excess compared to MinD (Fig. 2D, Movie S2). In the spiral phase, a rotating wavefront propagates from a well-defined core. The spirals are motile, annihilate when the cores of two counter-rotating spirals meet (Fig. S5A), and nucleate in counter-rotating pairs from a locally spiral-free background (Fig. S5B). The coexistence phase, which dominates at intermediary concentrations of MinDE, corresponds to a coexistence of the previously described two phases, with spatially restricted high-amplitude short-wavelength traveling waves propagating from the core of low-amplitude large-wavelength spiral waves (Fig. 2C and Movie S3). The spatially restricted planar wave patterns are highly dynamical and short-lived. They appear to form because of an instability at the core of the spiral wave where the MinD density is maximum, that, momentarily and locally, brings the system into the traveling-wave regime of the MinDE phase space (Fig. 2E). Diffusion eventually smooths the amplitude of the wave, effectively confining the traveling waves close to the core of the spirals. Statistical analysis of the MinD fluorescence intensity confirms the distinctness of the two coexisting patterns Fig. S5).

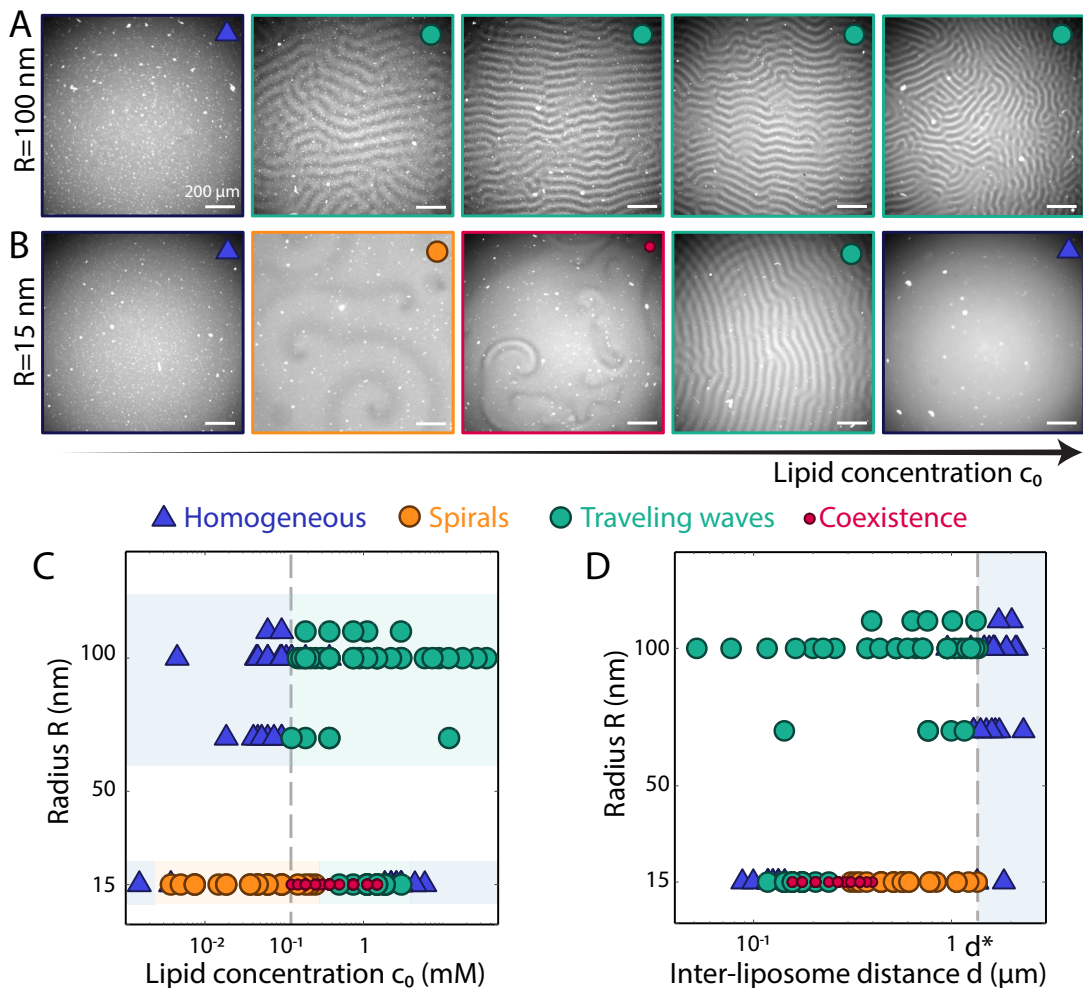


FIG. 3. **The properties of the liposomes suspension regulate pattern formation.** (A)-(B) Experimental MinD fluorescence images for two liposomes radius ((A): $R = 100 \text{ nm}$, (B): $R = 15 \text{ nm}$), at increasing lipid concentration c_0 (from left to right). Scale bar: $200 \mu\text{m}$. (C) Phase diagram in (R, c_0) , where R is the mean liposome's radius and c_0 the lipid concentration. Colored backgrounds represent regions of predominance of each type of patterns. (D) Phase diagram in (R, d) where d is the typical distance between two liposomes. The blue region indicates the region where no pattern form. The dashed line indicates the critical inter-liposome distance d^* above which no patterns form. For (C) and (D), each experiment was replicated two to five times. For all the experiments reported in this figure, proteins concentrations were fixed to $[\text{MinD}] = 3.8 \mu\text{M}$ and $[\text{MinE}] = 5.5 \mu\text{M}$.

IV. LIPOSOME SIZE AND DENSITY CONTROL PATTERN FORMATION

Varying the lipid concentration c_0 and the size distribution of the liposomes revealed that the properties of the dispersed substrate finely control the pattern-forming process. Starting with a suspension of liposomes with a mean radius of 15 nm and a fixed concentration of MinD and MinE, we observed that patterns only formed at intermediate lipid concentrations. As c_0 increases, the system transitions from a homogeneous state to spirals, coexistence, traveling waves and finally back to a homogeneous phase (Fig. 3A). Interestingly, sweeping across lipid concentrations for a different mean radius, $R \sim 70 \text{ nm}$ reveals that this critical concentra-

tion is size-dependent. Furthermore, changing the size also changes the variety of observed patterns, with only traveling waves forming at the larger liposome size (Fig. 3B). The existence of the spiral and coexistence phases is restored with larger liposomes by modifying protein concentration (Fig. S6). These observations highlight the complex dependence of the existence and nature of the pattern formed, particularly upon changes in liposome size, lipid concentration, and MinDE concentrations.

In particular, we observed that the average inter-liposome spacing d , which depends on the lipid concentration c_0 and size R (see Methods), governed a sharp transition (Fig. 3C) with a critical cutoff spacing $d^* \sim 1.5 \mu\text{m}$, above which patterns do not form irrespective of the liposome radius R (Fig. 3D). We conclude

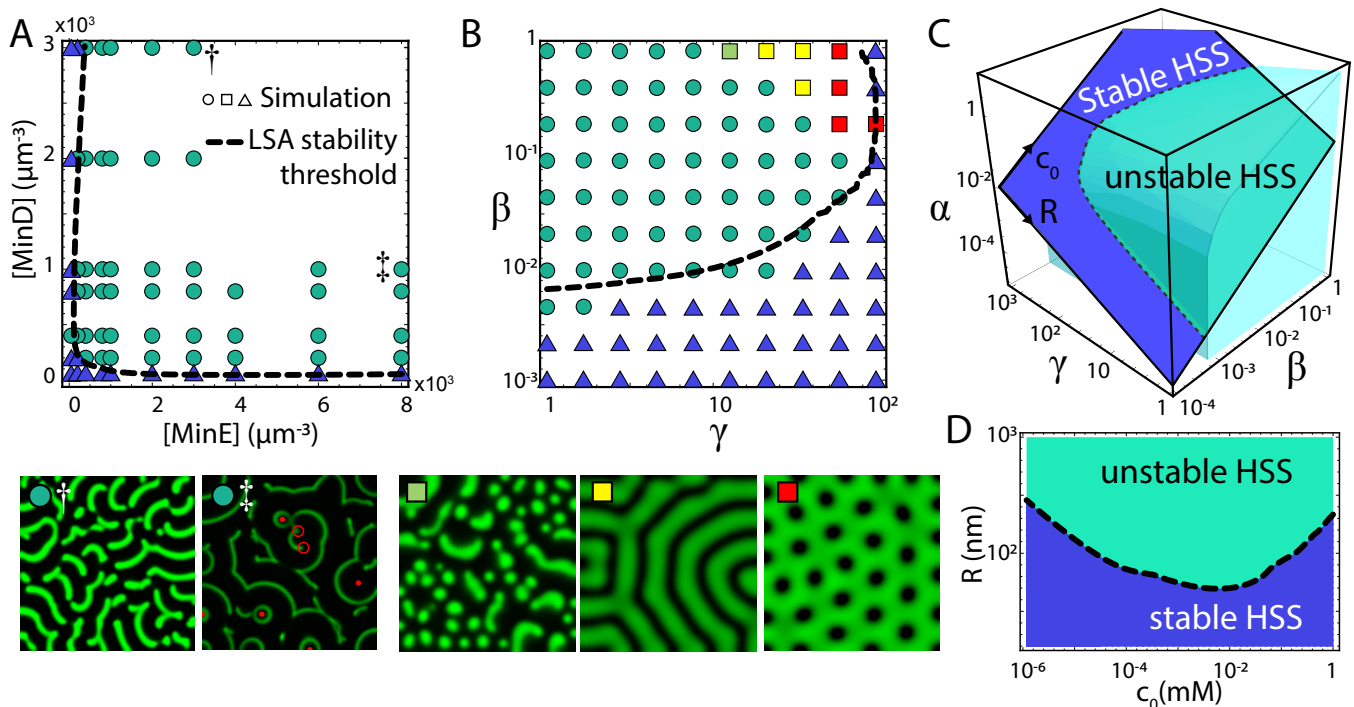


FIG. 4. **Model predictions depend on membrane properties and protein concentrations.** (A) $([\text{MinE}], [\text{MinD}])$ phase diagram with $\beta = 1$, $\gamma = 1$, and $\alpha = 1 \mu\text{m}^{-1}$ shows the dominance of wave states (teal circles) with homogeneous stationary states (blue triangles) occupying either low $[\text{MinE}]$ or low $[\text{MinD}]$ compositions; insets show two typical wave patterns, (\dagger) plane wave-dominated and (\ddagger) a state populated with targets (closed red point) and spirals (open red points). (B) (γ, β) phase diagram shows the emergence of various stationary patterns (red, yellow, and orange squares) and mixed-mode states (green squares) for $[\text{MinE}] = 1000$, $[\text{MinD}] = 800$ and $\alpha = 1 \mu\text{m}^{-1}$. In both (A) and (B), the dashed black lines correspond to linear stability analysis (LSA) prediction. (C) LSA predictions (patterns form in the teal volume) as a function of all three control parameters α, β and γ . The map between these three control parameters and the liposome size R and total lipid concentration c_0 , $\{\alpha(c_0), \beta(R, c_0), \gamma(R)\}$, is shown as the embedded surface with colors indicating stability. The intersection of the unstable region and this surface is shown in (D), where it is parameterized by R and c_0 in experimental units. For all simulation images, the domain width is $50 \mu\text{m}$.

from these observations that liposome size and concentration systematically control the nature and appearance of MinDE patterns. To further disentangle the impact of the various lipid properties on the dynamics and patterns formed and draw predictions on their role in the formation and nature of the patterns, we next turned our attention to the analysis of a theoretical model.

V. A 3D REACTION-DIFFUSION MODEL REVEALS THAT LIPOSOME DIFFUSIVITY AND DENSITY CONTROL PATTERN FORMATION.

To identify what characteristics of the dispersed membrane are important for controlling pattern formation, we modified a well-established 2D-3D PDE model [36] of MinDE where proteins react and bind to a 2D membrane while unbound proteins diffuse in 3D above the membrane. In our revised model, we considered a homogeneous medium in which bound and unbound proteins diffuse and react in 3D. The four main features of our

model are: *i*) we coarse-grained the liposomes and assumed that the membrane is homogeneously distributed, *ii*) we converted all the protein-bound surface concentrations into volumetric concentrations, *iii*) we replaced all the boundary flux terms for proteins binding with the membrane with volumetric sources and sinks, and *iv*) we allowed for increased diffusivity of all membrane-bound species to account for the fact that their transport is dominated by liposome mobility and not their local on-membrane diffusivity. During this process, we introduced three parameters α, β and γ . α [units: μm^{-1}] is the surface density of the membrane and naturally arises from converting surface concentrations into volumetric ones. We introduced the dimensionless on-rate reduction factor $\beta \in (0, 1]$ to phenomenologically account for the probability of co-localizing an unbound protein with the coarse-grained membrane. This is not required when the membrane is explicitly modeled through boundary conditions but is needed here because each volume element is only partially occupied by lipid binding sites. Finally, the dimensionless diffusivity scaling factor $\gamma > 1$, modulates

the diffusion coefficient of all membrane-bound proteins and complexes.

The model and its free parameters provide a framework for interpreting our experimental results. Critically, parameters α, β and γ collectively depend non-trivially on the size and the density of the liposomes. We first present simulation results in which we directly tuned α, β , and γ , and then outline how to connect these parameters to the experimental variables.

To develop a baseline understanding of the model's dynamics, we first identified the pattern-forming region of phase space by systematically varying the total concentrations of MinD and MinE, and comparing the phase diagram to the phase boundaries obtained from a linear stability analysis. At low diffusivity ($\gamma=1$), traveling waves dominate the pattern-forming region. The morphological and dynamical character of the patterns changed with the total protein concentrations. In the most common formation, the simulation box was filled with multiple ordered domains consisting of planar waves propagating in a time-persisting direction (Fig. 4A). The boundaries between these domains consisted of lines of phase singularities. Having an excess of MinE over MinD induced qualitative changes to the pattern, and target and spirals were readily detected (Fig. 4B). Patterns disappeared below a critical concentration of either MinD or MinE; the phase boundary measured from the PDE simulations coincided well with the prediction from linear stability analysis (dashed line in Fig. 4A).

Next, we explored the impact of membrane-dependent parameters α, β and γ on pattern formation using a combination of simulations and linear stability analysis. Fig. 4B considers the dynamics over a range β and γ for fixed protein composition. Increasing the diffusivity factor γ inhibited pattern formation, while increasing the binding rate factor β had the opposite effect, destabilizing the homogeneous medium and promoting pattern formation. Interestingly, for $\beta \sim 0.1 - 1$ as γ was increased, Min proteins formed various stationary Turing patterns, including stripes, honeycombs, and, for other concentrations of MinE and MinD, spots, en route to the homogeneous stationary state. At the transition between stationary and dynamic patterns, we observed mixed states, with quasi-stationary spots occupying the interface between regions exhibiting coherent waves (Fig. S7). The stability threshold in Fig. 4B depends on the membrane surface density α as well; Fig. 4C summarizes the full phase space predicted from linear stability analysis, with the volume enclosed by the teal surface demarcating the pattern-forming region. It shows that increasing the membrane surface density α counter-balances the destabilizing impact of β leading to another phase space domain with homogeneous steady state. Interestingly, we do not predict a loss of patterns at low α . However, we have not yet accounted for the interconnectedness of these three parameters.

Equipped with these observations, we next endeavored to qualitatively compare experiments and theory by re-

lating the model parameters α, β, γ to the experimental control parameters: the total lipid concentration c_o and the mean liposome size R . First, we find from geometric arguments that the membrane surface density α is proportional to the lipid concentration and independent of R . Second, the Stokes-Einstein relation shows that γ is inversely proportional to R and is independent of c_o . Finally, we posit that β , our binding rate reduction factor, follows the law of mass action and scales with liposome number density through $\beta \sim \mathcal{N}$. Thus, as the liposome suspension gets more dilute, the effective reaction rates for the binding of bulk-diffusing proteins to the membrane decrease. We arrive at $\beta = R\alpha(2/\pi)$, using our definition of α to simplify the expression by removing lipid concentration. To determine the prefactor, we have further assumed $\beta \rightarrow 1$, as the liposome density approaches the density at which average center-to-center $d \rightarrow 2R$ (see Supplementary Information). In fine, we have created a map between two experimental control parameters and our three simulation parameters: $\{R, c_o\} \leftrightarrow \{\alpha(c_o), \beta(R, c_o), \gamma(R)\}$.

We can now use this mapping to transform our theoretical results and facilitate comparison with experiments. Fig. 4C represents the map as a $\{R, c_o\}$ -parameterized plane embedded in the simulation parameter volume. The plane intersects with the linear stability analysis-predicted phase boundary (teal surface), highlighting the experimentally accessible pattern-forming regime. The black dashed line emphasizes the stability threshold on this subspace. To make further contact with the experiment, we re-plot the phase behavior from this slice in Fig. 4D. Notably, for intermediate liposome size, the diagram displays re-entrant behavior with respect to concentration. We find that pattern forms only for intermediary lipids concentrations. These critical concentrations depend on liposome size; increasing their radius increases the range of lipid concentrations where patterns form, consistent with our experimental observations (Fig. 3D).

VI. WAVELENGTH SELECTION DEPENDS ON PHYSICAL PARAMETERS OF THE DISPERSED MEMBRANE.

We have identified that the spacing between reaction sites and their mobility are two key parameters controlling the emergence of pattern formation. We next investigated the quantitative impact of these physical parameters on wavelength selection, focusing on the traveling wave regime.

At fixed liposome size, increasing the inter-liposome spacing by decreasing the lipid concentration induces an increase of the wavelength (red dots in Fig. 5A). Linear stability analysis predicts that increasing β , which increases binding kinetics, similarly decreases the wavelength (Fig. 5B). These predictions are also consistent with previous numerical studies on the 2D-3D system, which independently varied the binding rates k_d and k_{dD}

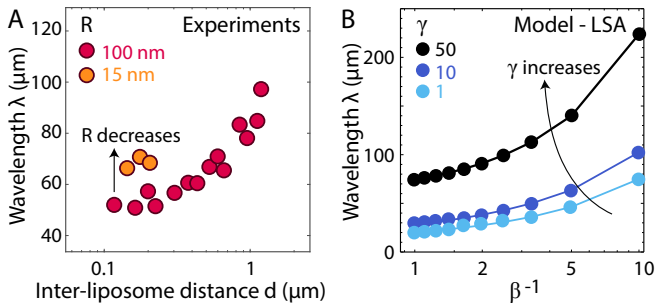


FIG. 5. **Wavelength depends on dispersed membrane properties.** (A) The wavelength λ increases when the inter-liposome distance d increases and decreases when the mean liposomes radius R decreases. Orange and red data points respectively correspond to: $R = 15 \text{ nm}$ and $R = 100 \text{ nm}$. Each data point is averaged over 2-5 replicates. Error bars are smaller than the marker size. (B) Linear stability analysis-predicted wavelength as a function of β^{-1} for $\gamma = \{1, 10, 50\}$, respectfully light blue, blue, and black.

that, in our model, both scale with β [38]. Finally, holding inter-liposome spacing constant while decreasing the liposome size R led to an increase of the wavelength, Fig. 5A (orange points). These observations are consistent with our model as well, where increasing diffusivity by increasing γ increases the wavelength (Fig. 5B).

Intuition for the opposing roles of reactive and diffusional processes on wavelength can be garnered by considering a dimensionless reaction-diffusion lengthscale $\sim \sqrt{\gamma\beta^{-1}}$, constructed from the scaling prefactors introduced in our model. While the numerical trends do not follow this scaling precisely, this quantity provides a rule of thumb for interpreting the results: diffusion tends to increase both the width of the reaction fronts and the pattern wavelength while increasing reaction rates tends to decrease these lengthscales. Overall, we conclude that the liposome properties impact both diffusive and reactive aspects of the Min system. The coarse-grained model enables us to disentangle these multiple influences, explaining the impact of lipid concentration and liposome size on the phase boundaries and on the emergent length-scale.

VII. CONCLUSION AND DISCUSSION

In summary, we revealed how the physical properties of a dispersed membrane control the formation of dynamical protein patterns by shifting the balance of reaction and diffusional processes. Changing the lipid concentration and size distribution of the liposomes offers a novel route for controlling the effective membrane binding rates and the diffusivity of membrane-bound proteins. This enables access to various dynamical 3D patterns and the modulation of their wavelength without changing the biochemistry of the constituent proteins themselves.

The dispersed membrane acts as a third reactive-diffusive specie that modulates the oscillatory behavior of MinE and MinD. Thus, we conclude that while membrane continuity might be required for MinDE to perform its function of localizing MinC and FtsZ *in vivo*, it is not necessary for pattern formation. Finally, the dispersed nature of the membrane enables the formation of space-filling three-dimensional protein patterns, opening up new opportunities for future studies of self-organization in 3D.

Our model qualitatively predicts the criteria for pattern formation and decouples lipid's multifaceted influence on dynamics into reactive and diffusive contributions. Through our comparison, we also identified limitations that may inspire future joint theory-experiment investigations. First, we note that the model presented here predicts that patterns will form under membrane conditions more dilute (low β and low α) than experimentally observed. We postulate that this is due to a breakdown in liposome synchronization in the experiment, which does not occur in our simulations. By coarse-graining the membrane, our model implicitly assumes that the state of all liposomes within a material element are well-described by a mean. However, it is possible that dynamics are locally oscillatory but not synchronized. Indeed, the experiments clearly show the existence of a critical inter-liposome spacing $d^* \sim 1.5 \mu\text{m}$ above which, patterns cannot form. We rationalize the existence of this critical inter-liposome spacing by considering published experimental and theoretical work on the MinDE oscillations [36]. After triggering the ATP hydrolysis by MinD, recently detached MinE exists in a transient activated conformation with a high affinity for membrane-bound MinD. If the activated MinE does not re-bind quickly enough, it will transform into a latent conformation with a lower affinity. The characteristic length scale associated with the active MinE can be estimated as $l_E = \sqrt{\frac{D_c}{\mu}} \sim 0.77 \mu\text{m}$, where $D_c = 60 \mu\text{m}^2 \cdot \text{s}^{-1}$ is the diffusivity of unbound MinE and $\mu = 100 \text{ s}^{-1}$ is the active-to-latent conformational switch rate [36]. If the inter-liposome spacing d is smaller than l_E , then MinE mostly exists in its activated confirmation and can readily re-bind to a neighboring liposome. If the inter-liposome spacing d is larger than l_E , then MinE will go back to its lower reactive state before finding another liposome, and pattern will not form. This interpretation is consistent with our experimental findings: no spatially extended patterns form above a critical inter-liposome spacing. However, in that regime, individual liposomes still display periodic temporal oscillations (Fig. S8), demonstrating that MinDE maintains the ability to oscillate under dilute conditions, as predicted by the model, but the oscillations cannot synchronize to form extended patterns.

Second, at high diffusivity γ and high β , our model consistently predicts the formation of a variety of static Turing patterns, which to date were observed only marginally in our experiments (Fig. S9). Future work

should focus on testing this theoretical prediction more robustly by further reducing the liposome’s mean radius and increasing their concentration.

Finally, our experiments clearly show that two distinct dynamical patterns can form; one characterized by closely packed traveling waves and another by isolated spirals. The distinction between the two is most apparent in the coexistence phase, where short-lived spatially restricted traveling waves form at the core of the spiral wave cores. By contrast, simulations exhibit a more continuous transition between packed plane waves and those possessing more clear spirals; however, even in these cases, the spirals are more densely packed than in the experiment (see insets of Fig. 4A[†], [‡]). The spiral waves obtained in the 3D MinDE system are reminiscent of scroll waves seen in chemical and biological 3D excitable media, including the Belousov–Zhabotinsky reaction [39] and cardiac tissues [40, 41]. Spirals are readily observed when Min proteins form pattern on a flat 2D membrane [9]. However, the core of the 2D spirals are, to the best of our knowledge, largely pinned to specific locations on the membrane once established. In 3D, the spiral cores are motile and we observed multiple annihilation and creation events of counter-rotating spirals. The dispersed Min system will allow further experimental investigation of how dimensionality impacts defects dynamics in pattern-forming systems [42].

The absence of these dynamical states in our model opens exciting opportunities to investigate their origin. We formulate below a few hypotheses that could be tested experimentally or theoretically. First, it is possible that some of the model parameters, including the chemical rates and diffusivity of the various proteins, can be further optimized. It may be appropriate to measure, when possible, the binding rates of MinDE onto liposomes instead of relying on published estimates and measurements for proteins binding on a flat, continuous membrane. A second but related extension is to consider in the model the possibility that membrane curvature impacts binding rates [43, 44]. Third, the spiral phase identified experimentally could actually result from the combined effects of excitability and noise near phase transitions. The theoretical model shows indeed a sudden emergence of large-scale oscillations consistent with the experiments, which is evocative of excitable media [45]. Heterogeneity and stochastic fluctuations near sudden transitions are known to promote complex pattern formation or attractor switching or resonances [46]. In our system, we know that the substrate is heterogeneous, given that the liposome suspension is polydispersed in size (Fig. S1). The highly dynamical spirals and coexistence states observed experimentally could be a signature of the sudden transitions associated with the nonlinearities and excitability of the system, added to heterogeneous fluctuations. Future work should be focused on distinguishing between these different scenarii.

Our findings have broad implications in biology, nonequilibrium materials, and dynamical systems for two

reasons. First, the Min system is a prototypical example of ATPase/nucleotide binding reactions, which are crucial for many cellular processes. Second, intracellular pattern formation on dispersed substrate is ubiquitous in biology, from the ParA/B proteins that bind to a circular bacterial DNA plasmid packed in a random 3D coil [10], to chemomechanical excitability of the actin cortex in *C. Elegans* [12, 47, 48], *Drosophila* embryos [49–51], and in *Xenopus* [14, 16, 52] and Starfish oocyte [15, 53, 54]. These two protein pattern-forming systems are relevant because their binding substrate - respectively a linear strand of DNA or an actin filament - is small compared to the size of the pattern, can diffuse in 3D, and is diffusively coupled through the cytoplasm. Our work suggests that cells could modify the density and diffusivity of their dispersed substrates to modulate pattern formation without changing their protein binding biochemistry.

Finally, we want to conclude this article by highlighting once again the multiscale nature of the phenomena studied here. Dynamic pattern will still form if the membrane is fragmented into diffusive liposomes of typical size 15 nm and spacing 500 nm, respectively three and two orders of magnitude smaller than the pattern lengthscale ($\sim 100\mu\text{m}$). However, our model predicts that fragmenting the membrane even further will prevent pattern formation because of the high diffusivity of the substrate. Fragmenting the membrane uniquely enables the formation of 3D patterns that exhibit new dynamics not found for patterns forming on 2D membranes. This work further establishes the Min system as a paradigmatic *in vitro* model to study biological self-organization in 3D, despite only exhibiting 2D patterns *in vivo*.

Acknowledgments. We thank Pr. Petra Schwille and Dr. Michaela Schaper for the His-MinE plasmid. We thank Dr. Shibani Dalal, Director of the Brandeis Biomaterial Facility for help with protein purification. We also thank Dr. Joseph Lopes, Lance Babcock, and Dr. Bibi Najma for initial work on the 2D Min system. This work was supported by the Brandeis NSF Materials Research Science and Engineering Center (MRSEC) Grant No. DMR-2011846. G.D. acknowledges support from NSF CAREER Grant No. DMR-2047119. We also acknowledge the use of the optical and biomaterial facilities supported by NSF MRSEC Grant No. DMR-2011846.

Appendix A: PDE Model

We adapt a PDE model of MinDE dynamics that tracks the spatiotemporal dynamics of various forms of membrane-bound and freely-diffusing “bulk” MinD, MinE, and MinD-MinE complexes [36]. The model accounts for the interrelated dynamics of 7 species in total, 4 in the cytosol and 3 on the membrane. Beginning in the cytosol, we have two forms of MinD, those bound to ATP u_{DT} and those bound to ADP u_{DD} , and two forms of MinE, a “reactive” form u_{ER} that binds rapidly

to membrane-bound MinD, and a slower-reacting “latent” form u_{EL} . On the membrane, MinD u_d , MinE, and MinD-MinE u_{de} complexes are tracked. Following the convention from Refs. [36, 55] and others, capital subscripts denote cytosolic species, where lowercase indicate membrane-bound. The units of these species are inherited from the dimension of their domain: all bulk fluid species are in units of $[\#/ \mu\text{m}^3]$ with membrane-bound in $[\#/ \mu\text{m}^2]$. We begin by restating the 2D membrane and 3D bulk equations with appropriate reactive bound conditions coupling them:

$$\partial_t u_{DD} = D_c \nabla^2 u_{DD} - \lambda_{DD} u_{DD} \quad (\text{A1})$$

$$\partial_t u_{DT} = D_c \nabla^2 u_{DT} + \lambda_{DD} u_{DD} \quad (\text{A2})$$

$$\partial_t u_{ER}^r = D_c \nabla^2 u_{ER}^r - \mu u_{ER}^r \quad (\text{A3})$$

$$\partial_t u_{EL}^l = D_c \nabla^2 u_{EL}^l + \mu u_{ER}^r \quad (\text{A4})$$

$$\partial_t u_d = D_d \nabla^2 u_d + (k_D + k_{dD} u_d) u_{DT}|_{\partial\Omega} - u_d (u_{ER}^r|_{\partial\Omega} k_{dE}^r + u_{EL}^l|_{\partial\Omega} k_{dE}^l) - k_{ed} u_d u_e \quad (\text{A5})$$

$$\partial_t u_{de} = D_{de} \nabla^2 u_{de} + u_d (u_{ER}^r|_{\partial\Omega} k_{dE}^r + u_{EL}^l|_{\partial\Omega} k_{dE}^l) - k_{de} u_{de} + k_{ed} u_d u_e \quad (\text{A6})$$

$$\partial_t u_e = D_e \nabla^2 u_e + k_{de} u_{de} - k_{ed} u_d u_e - k_e u_e \quad (\text{A7})$$

$$(\text{A8})$$

These 2D and 3D PDE's are coupled through the following boundary fluxes $f_{\partial\Omega}$:

$$D_c \mathbf{n} \cdot \nabla u_{DD}|_{\partial\Omega} = k_{de} u_{de} \quad (\text{A9})$$

$$D_c \mathbf{n} \cdot \nabla u_{DT}|_{\partial\Omega} = -(k_D + k_{dD} u_d) u_{DT} \quad (\text{A10})$$

$$D_c \mathbf{n} \cdot \nabla u_{ER}^r|_{\partial\Omega} = -k_{dE}^r u_d u_{ER}^r + k_e u_e \quad (\text{A11})$$

$$D_c \mathbf{n} \cdot \nabla u_{EL}^l|_{\partial\Omega} = -k_{dE}^l u_d u_{EL}^l \quad (\text{A12})$$

Given the separation of length scales between the size of liposomes $\sim \mathcal{O}(10 - 100)$ [nm] and that of typical patterns $\sim \mathcal{O}(100)$ [μm], we develop a continuum model by coarse-graining away the fine features of the liposomes. Each volume element in our model contains an concentration of lipids c_o arranged into liposomes of size R and a mix of free and membrane-bound proteins but disregards detailed dynamics on and between liposomes.

To begin, we first transform the membrane concentrations with units $[\#/m^2]$ to volumetric concentrations. We consider a volume element with volume V containing lipid with a surface area A . The total number of bound proteins is then $N = Au$. Dividing by the volume gives the volumetric concentration $u^* = \frac{A}{V} u \equiv \alpha u$ or $u = \alpha^{-1} u^*$. This conversion will be applied to all surface-bound species $\{u_d, u_{de}, u_e\}$. Similarly, the surface fluxes

$f_{\partial\Omega}$ Eqns. 8-10 can be converted to volumetric source terms f_Ω in Eqns. 1-3 by assuming that such fluxes act over the same effective area A and then dividing by V to find the rate of change per time per volume. Thus $f_\Omega = \frac{A}{V} f_{\partial\Omega} \equiv \alpha f_{\partial\Omega}$.

Additionally, we note that in Eqns. 8-10, u_{DT} and u_E represent the activated minD and minE concentrations at the membrane. In our dispersed membrane model, a given volume element contains a concentration of lipid upon which binding can occur. To account for the impact of liposome availability, we scale all bulk-to-membrane processes with $\beta \in (0, 1]$. Finally, we let the membrane-bound diffusivities be increased by a factor $\gamma > 1$ to account for the mobility of the liposomes to which these species are bound.

Combining these facts and simplifying gives the following bulk equations where all concentrations are in $[\#/m^3]$:

$$\partial_t u_{DD} = D_c \nabla^2 u_{DD} - \lambda_{DD} u_{DD} + k_{de} u_{de}^* \quad (\text{A13})$$

$$\partial_t u_{DT} = D_c \nabla^2 u_{DT} + \lambda_{DD} u_{DD} - (\beta \alpha k_D + \beta k_{dD} u_d^*) u_{DT} \quad (\text{A14})$$

$$\partial_t u_E^r = D_c \nabla^2 u_E^r - \beta k_{dE}^r u_d^* u_E^r + k_e u_e^* - \mu u_E^r \quad (\text{A15})$$

$$\partial_t u_E^l = D_c \nabla^2 u_E^l - \beta k_{dE}^l u_d^* u_E^l + \mu u_E^l \quad (\text{A16})$$

$$\partial_t u_d^* = \gamma D_d \nabla^2 u_d^* + (\beta \alpha k_D + \beta k_{dD} u_d^*) u_{DT} - \beta u_d^* (k_{dE}^r u_E^r + k_{dE}^l u_E^l) - \frac{1}{\alpha} k_{ed} u_d^* u_e^* \quad (\text{A17})$$

$$\partial_t u_{de}^* = \gamma D_{de} \nabla^2 u_{de}^* + \beta u_d^* (k_{dE}^r u_E^r + k_{dE}^l u_E^l) - k_{de} u_{de}^* + \frac{1}{\alpha} k_{ed} u_d^* u_e^* \quad (\text{A18})$$

$$\partial_t u_e^* = \gamma D_e \nabla^2 u_e^* + k_{de} u_{de}^* - \frac{1}{\alpha} k_{ed} u_d^* u_e^* - k_e u_e^* \quad (\text{A19})$$

parameter description	symbol	value
binding rate of bulk minD to membrane	k_D	0.0625
cooperative binding rate of minD to membrane-bound minD	k_{dD}	0.02
rate of reactive-minE recruitment from bulk to membrane-bound minD	k_{dEr}	0.2
rate of latent-minE recruitment from bulk to membrane-bound minD	k_{dEl}	0.002
rate of minDE complex degradation	k_{de}	0.34
rate of complex formation between membrane bound minE and minD	k_{ed}	0.01
membrane-bound minE off rate	k_e	0.01
minD recycling rate: ADP \rightarrow ATP	λ_{DD}	6
bulk minE inactivation rate	μ	100
average minD concentration	n_D	$\mathcal{O}(10^2 - 10^4) [\# / \mu\text{m}^{-3}]$
average minE concentration	n_E	$\mathcal{O}(10^2 - 10^4) [\# / \mu\text{m}^{-3}]$
diffusion coefficient for unbound MinD, MinE $\{u_{DT}, u_{DD}, u_{Er}, u_E\}$	D_c	60
diffusion coefficient of bound MinD (u_d)	D_d	0.013
diffusion coefficient of bound MinE (u_e)	D_e	0.005
diffusion coefficient of bound MinD-MinE (u_{de})	D_{de}	0.013
lipid surface area to volume ratio	α	$10^{-3} - 10^1 [\mu\text{m}^{-1}]$
bulk-to-membrane reaction rate reduction factor	β	$10^{-3} - 10^0 [-]$
diffusivity factor for membrane-bound proteins	γ	$10^0 - 10^3 [-]$

TABLE I. Table of model parameters

Appendix B: Experimental methods

1. Samples preparation

a. Proteins purification

His-MinD and His-MinE were purified using the plasmids pET28a-His-MinD-MinE, pET28a-eGFP-MinD and pET28a-MinE, respectively. The MinD plasmids were purchased from Addgene (https://www.addgene.org/Petra_Schwille/) and the His-MinE plasmid was gifted from the Schwille lab. In short, proteins were expressed in *E. Coli* BL21 pLysS and purified through a His-Trap Ni-NTA affinity column, following the detailed protocol published in [56]. Purified proteins were further

size-excluded in a storage buffer (50.0 mM HEPES/KOH at pH 7.2, 150.0 mM KCl, 10% glycerol, 0.1mM EDTA and 0.4mM tris(2-carboxyethyl)phosphine). Proteins were flash frozen in liquid nitrogen and stored in small aliquots at -80°C .

b. Protein labeling

The labeling of His-MinE with CF-568 maleimide (Biotium 92024) was performed according to the dye manufacturer's instructions. In brief, the protein stock solution was mixed with 3-fold molar excess of reactive dye. The reaction mixture was incubated for 2 h at room temperature protected from light. A spin desalting column (ThermoFisher, Zeba 7K MWCO, 0.5ml, Prod #89882)

was used to remove most of the unbound dye.

c. Measure of proteins concentration

Protein concentrations were determined using a linearized Bradford assay with bovine serum albumin as a reference. We used a NanoDrop Spectrophotometer and repeated measurements at least three times for each concentration.

d. Liposomes preparation

We prepare a solution of 70 mol% DOPC (Avanti, 18:1 (Δ 9-cis) PC; SKU, 850375C) and 30 mol% DOPG (Avanti, 18:1 (Δ 9-cis) PG, SKU: 840475C), dissolved in chloroform. Chloroform is then evaporated under a vacuum pump for 3h. The dry lipid film is rehydrated in Min buffer (25 mM Tris-HCl pH 7.5, 150 mM KCl, 5 mM MgCl₂) to a final lipid stock concentration of 5mM.

15 nm liposomes are prepared by using tip sonication at middle range power until clarity (\sim 3 min). Other sizes of liposomes (70 nm, 100 nm, 110 nm) are prepared using extrusion techniques, with appropriate porous membranes. Liposomes solutions are stored in 4°C for maximum two weeks.

Labeled liposomes are prepared using the same protocol, starting with a mixture of 69 mol% DOPC (Avanti, 18:1 (Δ 9-cis) PC; SKU, 850375P), 30 mol% DOPG (Avanti, 18:1 (Δ 9-cis) PG, SKU: 840475P) and 1 mol% Liss Rhod-PE (Avanti, 18:1, SKU: 810150C).

Size distribution, concentration and diffusion coefficient of each solution of liposomes were measured using Dynamic Light Scattering. Liposomes solution was diluted 1000x in Min buffer. Measurements were made at 25°C, using a 5 μ L cassette. We confirmed that the liposomes suspensions were stable over the two weeks time period of liposomes storage.

e. Sample preparation

In order to ensure time stability of our samples under image acquisition, we prepared our active mixture by diluting our stock proteins to the working concentration in Min buffer supplemented with ATP (final concentration 2.5 μ M), ATP regenerating system containing 26-mM Phosphoenolpyruvic acid monopotassium salt (PEP, Beantown Chemical, 129745) and pyruvate kinase and lactate dehydrogenase enzymes 2.8% v/v (PK/LDH, Sigma, P-0294), and antioxidants to reduce photobleaching (glucose 18.7 mM, DTT 5.5 mM, glucose oxidase 1.4 μ M, and catalase 0.17 μ M).

f. Microfluidic channels and sample loading

Our active mix was confined in rectangular flow channels. Our microfluidic device was assembled using two glass slides spaced by a layer parafilm (height \sim 100 μ m). The glass surfaces were coated with a PEG-acrylamide brush to prevent nonspecific protein adsorption. Parafilm spacers were cut following an home-made design on a cutting machine. They were then placed between the two glass surfaces and melted to 65 °C to ensure good adhesion to the glass surfaces.

Experiments performed with channels at different height used double-sided tape instead of parafilm spacers.

Samples of 8 μ L were loaded into each channel by capillarity using a micropipette. Finally, channels were sealed using a UV-curing optical adhesive (NOA 81, Norland Products Inc.) to ensure no external flow during the time of acquisition of the experiment.

2. Microscopy

a. Widefield fluorescence microscopy

Time-lapse image acquisitions were taken using a Nikon Eclipse Ti2 inverted fluorescence microscope, equipped with a LED light source (Lumencor sola 80-10244). The multiposition data acquisitions, the time interval between the images, exposure time, and illumination intensity were controlled by a micromanager software [57]. The typical delay between two successive images of the same field of view was set to be 30s. A Hamamatsu camera (ORCA4.0V1, pixel size 6.45 μ m) and a 4x or 10x objective (Nikon Plan Apo) were used for imaging Min proteins concentration field.

b. Confocal microscopy

3D visualisation of the patterns was obtained by volume reconstruction from z-slices images taken by confocal microscopy (Nikon AX-R). We used 10x or 20x objectives. Samples were illuminated using the appropriate wavelength (488nm for MinD-gfp and 561nm for CF568-MinE or rhodamine labelled lipids) from the light source. The step size was set to 2 μ m and time interval between two images to 30 s, both ensuring sufficient resolution in time and space to avoid loss of information on the dynamics or structure, without introducing any bias of dynamics between two z slices.

3. Image and data analysis

Patterns characterization: The type of patterns for each experiment is determined manually, following

the criteria given in the main text (Fig. 2).

Kymographs and intensity profiles: we used ImageJ to reshape our images as space-time kymograph and extract the intensity profiles values. The intensity was normalized as: $(I - \langle I \rangle) / \langle I \rangle$.

Wavelength and period: We measured wavelength and period using a handmade automatized Matlab code. Briefly, we reshape intensity images into space-time kymographs along x or y slices. We then perform spatial (resp. temporal) autocorrelation function and detect the wavelength (resp. period) as the 1st maxima. The wavelength and period final values are averaged over 25 x-slices and 25 y-slices.

Phase field and defects: To extract the positions of the core of the spirals, we measured the local winding number in the phase field. The phase field is computed following protocol given in [15]. Clockwise (resp.

anti-clockwise) spirals correspond to a winding number equals to +1 (resp. -1).

Liposomes suspension parameters: to generate our phase diagrams, we derived the inter-liposome distance d from the measured average radius R and concentration c_0 , from Dynamical Light Scattering as explained in the previous section. Using formulas in [58], we estimate the number of liposomes per unit volume as:

$$\mathcal{N}_{liposomes} [\#/mL] = \frac{c_0 a \mathcal{N}_A}{4\pi (R^2 + (R-h)^2) * 10^3} \quad (B1)$$

where \mathcal{N}_A is Avogadro's number, $a = 0.7 \text{ nm}^2$ is the area of a single lipid head, and $h \sim 5 \text{ nm}$ is the thickness of the lipid membrane.

Then, the inter-liposome distance is defined as

$$d = (\mathcal{N}_{liposomes})^{-1/3} - 2R. \quad (B2)$$

-
- [1] A. M. Turing, *Bulletin of mathematical biology* **52**, 153 (1990).
- [2] A.-J. Koch and H. Meinhardt, *Reviews of modern physics* **66**, 1481 (1994).
- [3] J. Halatek, F. Brauns, and E. Frey, *Philosophical Transactions of the Royal Society B: Biological Sciences* **373**, 20170107 (2018).
- [4] D. M. Raskin and P. A. J. de Boer, *Proceedings of the National Academy of Sciences* **96**, 4971 (1999), <https://www.pnas.org/doi/pdf/10.1073/pnas.96.9.4971>.
- [5] R. Rajasekaran, C.-C. Chang, E. W. Weix, T. M. Galanteo, and S. M. Coyle, *Cell* **187**, 345 (2024).
- [6] T. H. Szeto, S. L. Rowland, C. L. Habrukowich, and G. F. King, *Journal of Biological Chemistry* **278**, 40050 (2003).
- [7] Z. Hu and J. Lutkenhaus, *Molecular Cell* **7**, 1337 (2001).
- [8] K. C. Huang, Y. Meir, and N. S. Wingreen, *Proceedings of the National Academy of Sciences* **100**, 12724 (2003), <https://www.pnas.org/doi/pdf/10.1073/pnas.2135445100>.
- [9] M. Loose, E. Fischer-Friedrich, J. Ries, K. Kruse, and P. Schwille, *Science* **320**, 789 (2008), <https://www.science.org/doi/pdf/10.1126/science.1154413>.
- [10] B. Etemad-Moghadam, S. Guo, and K. J. Kempfues, *Cell* **83**, 743 (1995).
- [11] S. Ringgaard, J. van Zon, M. Howard, and K. Gerdes, *Proceedings of the National Academy of Sciences* **106**, 19369 (2009).
- [12] N. W. Goehring, P. K. Trong, J. S. Bois, D. Chowdhury, E. M. Nicola, A. A. Hyman, and S. W. Grill, *Science* **334**, 1137 (2011), <https://www.science.org/doi/pdf/10.1126/science.1208619>.
- [13] R. Ietswaart, F. Szardenings, K. Gerdes, and M. Howard, *PLoS computational biology* **10**, e1004009 (2014).
- [14] W. M. Bement, M. Leda, A. M. Moe, A. M. Kita, M. E. Larson, A. E. Golding, C. Pfeuti, K.-C. Su, A. L. Miller, A. B. Goryachev, and G. von Dassow, *Nat Cell Biol.* **17**, 1471 (2015).
- [15] T. H. Tan, J. Liu, P. W. Miller, M. Tekant, J. Dunkel, and N. Fakhri, *Nature Physics* **16**, 657 (2020).
- [16] S. Chen, D. S. Seara, A. Michaud, S. Kim, W. M. Bement, and M. P. Murrell, *Nature Physics* , 1 (2024).
- [17] A. G. Vecchiarelli, M. Li, M. Mizuuchi, and K. Mizuuchi, *Molecular Microbiology* **93**, 453 (2014), <https://onlinelibrary.wiley.com/doi/pdf/10.1111/mmi.12669>.
- [18] P. Glock, B. Ramm, T. Heermann, S. Kretschmer, J. Schweizer, J. Mücksch, G. Alagöz, and P. Schwille, *ACS Synthetic Biology* **8**, 148 (2019).
- [19] B. Ramm, P. Glock, J. Mücksch, P. Blumhardt, D. A. García-Soriano, M. Heymann, and P. Schwille, *Nature Communications* **9**, 3942 (2018).
- [20] B. Ramm, A. Goychuk, A. Khmelinskaia, P. Blumhardt, H. Eto, K. A. Ganzinger, E. Frey, and P. Schwille, *Nature Physics* **17**, 850 (2021).
- [21] S. Gavrilović, G. A. Brüggenthies, J. M. Weck, A. Heuer-Jungemann, and P. Schwille, *Small* **20**, 2309680 (2024).
- [22] M. Fu, T. Burkart, I. Maryshev, H. G. Franquelim, A. Merino-Salomón, M. Reverte-López, E. Frey, and P. Schwille, *Nature Physics* **19**, 1211 (2023).
- [23] V. K. Vanag and I. R. Epstein, in *Self-Organized Morphology in Nanostructured Materials*, Vol. 99, edited by R. Hull, R. M. Osgood, J. Parisi, H. Warlimont, K. Al-Shamery, and J. Parisi (Springer Berlin Heidelberg, Berlin, Heidelberg, 2008) pp. 89–113, series Title: Springer Series in Materials Science.
- [24] I. R. Epstein, V. K. Vanag, A. C. Balazs, O. Kuksenok, P. Dayal, and A. Bhattacharya, *Accounts of Chemical Research* **45**, 2160 (2012).
- [25] V. Castets, E. Dulos, J. Boissonade, and P. De Kepper, *Physical Review Letters* **64**, 2953 (1990).
- [26] I. Lengyel and I. R. Epstein, *Science* **251**, 650 (1991).
- [27] J. Halatek and E. Frey, *Nature Physics* **14**, 507 (2018).
- [28] F. Brauns, G. Pawlik, J. Halatek, J. Kerssemakers, E. Frey, and C. Dekker, *Nature Communications* **12**, 3312 (2021).
- [29] F. Brauns, J. Halatek, and E. Frey, *Physical Review Research* **3**, 013258 (2021).

- [30] L. Würthner, F. Brauns, G. Pawlik, J. Halatek, J. Kersse-makers, C. Dekker, and E. Frey, *Proceedings of the National Academy of Sciences* **119**, e2206888119 (2022), <https://www.pnas.org/doi/pdf/10.1073/pnas.2206888119>.
- [31] R. Geßele, J. Halatek, L. Würthner, and E. Frey, *Nature Communications* **11**, 539 (2020).
- [32] H. J. e. a. Brauns F., Pawlik G., *Nat Commun* (2021), [10.1038/s41467-021-23412-5](https://doi.org/10.1038/s41467-021-23412-5).
- [33] J. Schweizer, M. Loose, M. Bonny, K. Kruse, I. Monch, and P. Schwille, *Proceedings of the National Academy of Sciences* **109**, 15283 (2012), ISBN: 1091-6490 (Electronic)\r0027-8424 (Linking).
- [34] V. W. Rowlett and W. Margolin, *Current Biology* **23**, R553 (2013).
- [35] J. Denk, S. Kretschmer, J. Halatek, C. Hartl, P. Schwille, and E. Frey, *Proceedings of the National Academy of Sciences* **115**, 4553 (2018).
- [36] J. Denk, S. Kretschmer, J. Halatek, C. Hart, P. Schwille, and E. Frey, *PNAS* (2018).
- [37] M. Loose, E. Fischer-Friedrich, C. Herold, K. Kruse, and P. Schwille, *Nature Structural & Molecular Biology* **18**, 577 (2011).
- [38] Z. Ren, H. Weyer, L. Würthner, D. Li, C. Sou, D. Villarreal, E. Frey, and S. Jun, *bioRxiv* (2023), [10.1101/2023.08.15.553443](https://doi.org/10.1101/2023.08.15.553443).
- [39] T. Bánsági, V. K. Vanag, and I. R. Epstein, *Science* **331**, 1309 (2011).
- [40] M. F. ARNSDORF and J. C. MAKIELSKI, in *Heart Physiology and Pathophysiology (Fourth Edition)*, edited by N. SPERELAKIS, Y. KURACHI, A. TERZIC, and M. V. COHEN (Academic Press, San Diego, 2001) fourth edition ed., pp. 99–132.
- [41] Y. Wang, Q. Li, B. Tao, M. Angelini, S. Ramadoss, B. Sun, P. Wang, Y. Krokhaleva, F. Ma, Y. Gu, A. Espinoza, K. Yamauchi, M. Pellegrini, B. Novitch, R. Olcese, Z. Qu, Z. Song, and A. Deb, *Science* **381**, 1480 (2023), <https://www.science.org/doi/pdf/10.1126/science.adh9925>.
- [42] J. P. Keener, *Physica D: Nonlinear Phenomena* **31**, 269 (1988).
- [43] E. Mileykovskaya, I. Fishov, X. Fu, B. D. Corbin, W. Margolin, and W. Dowhan, *Journal of Biological Chemistry* **278**, 22193 (2003).
- [44] D. H. Johnson, O. H. Kou, N. Bouzos, and W. F. Zeno, *Trends in Biochemical Sciences* **49**, 401 (2024).
- [45] Of note, a simple model composed of two diffusively coupled homogeneous compartments revealed that i) increasing β leads to a sub-critical Hopf bifurcation, meaning that prior to the transition, the system is bistable and ii) the system is excitable.
- [46] D. Mittal and R. Narayanan, *Proceedings of the National Academy of Sciences* **119** (2022), [10.1073/pnas.2202962119](https://doi.org/10.1073/pnas.2202962119).
- [47] M. Nishikawa, S. R. Naganathan, F. Julicher, and S. W. Grill, *eLife* **6**, e19595 (2017).
- [48] J. B. Michaux, F. B. Robin, W. M. McFadden, and E. M. Munro, *Journal of Cell Biology* **217**, 4230 (2018).
- [49] A. C. Martin, M. Kaschube, and E. F. Wieschaus, *Nature* **457**, 495 (2009).
- [50] R. Fernandez-Gonzalez and J. A. Zallen, *Physical biology* **8**, 045005 (2011).
- [51] M. F. Staddon, E. M. Munro, and S. Banerjee, *PLOS Computational Biology* **18**, 1 (2022).
- [52] S. Hladyshau, M. Kho, S. Nie, and D. Tsygankov, *Scientific Reports* **11**, 19512 (2021).
- [53] J. Liu, J. F. Tetzlaff, P. W. Miller, A. D. Hastewell, Y.-C. Chao, J. Dunkel, and N. Fakhri, *Proceedings of the National Academy of Sciences* **118**, e2104191118 (2021), <https://www.pnas.org/doi/pdf/10.1073/pnas.2104191118>.
- [54] P. J. Foster, S. Fürthauer, and N. Fakhri, *bioRxiv* (2022), [10.1101/2022.04.22.489189](https://doi.org/10.1101/2022.04.22.489189).
- [55] M. Fu, T. Burkart, I. Maryshev, H. G. Franquelim, A. Merino-Salomón, M. Reverte-López, E. Frey, and P. Schwille, *Nat. Phys.* **19**, 1211–1218 (2023).
- [56] S. P. Ramm Beatrice, Glock Philipp, *JoVE* , e58139 (2018).
- [57] A. D. Edelstein, M. A. Tsuchida, N. Amodaj, H. Pinkard, R. D. Vale, and N. Stuurman, *J. Biol. Methods* **1** (2014), [10.14440/jbm.2014.36](https://doi.org/10.14440/jbm.2014.36).
- [58] M. R. Mozafari, E. Mazaheri, and K. Dormiani, *Scientia Pharmaceutica* **89** (2021), [10.3390/scipharm89020015](https://doi.org/10.3390/scipharm89020015).